

Supplementary Information 1

A ddPCR platform based on a microfluidic chip with a dual-function flow-focusing structure for sample-to-result DNA quantification analysis

1. The verification of the relationship between the evaporation situation and the temperature difference between air and liquid.

We verified that droplets are less susceptible to evaporation when the air temperature is greater than droplet temperature through both theoretical analysis and experimental verification.

Initially, the relationship of mass rate of evaporation j was found to be described as^{1, 2}:

$$j = \alpha \sqrt{\frac{M}{2\pi R}} \left(\frac{P_s(T_1)}{\sqrt{T_1}} - \frac{P_v}{\sqrt{T_v}} \right) \quad (\text{S1})$$

where M is the molecular weight of the vapor, R is the universal gas constant, P_s is the saturation pressure corresponding to the interfacial liquid-phase temperature T_1 , P_v and T_v are the vapor pressure and vapor temperature, respectively, and α is the accommodation evaporation coefficient.

The relationship between evaporation rate and temperature, pressure, and other factors is articulated in Equation S1, highlighting the usefulness of the referee's suggestion to estimate the pressure in the collecting tube is helpful to elucidate the phenomenon. Further, in order to make the referee more intuitive understanding of the relationship between evaporation rate and temperature, we use the linearized Hertz–Knudsen equation derived from kinetic theory to portray the relation between temperature difference between two sides of vapor-liquid interface and steady mass rate of evaporation³:

$$j = \alpha \rho_v h_{fg} \sqrt{\frac{M}{2\pi R T_v^3}} (T_1 - T_v) \quad (\text{S2})$$

where h_{fg} is the latent heat of evaporation and ρ_v is the density of the vapor. When $T_1 - T_v$ is less than zero, evaporation is suppressed. Therefore, the droplet evaporation is suppressed when the air temperature is greater than the highest droplet temperature which

is 98 °C during inactivation stage.

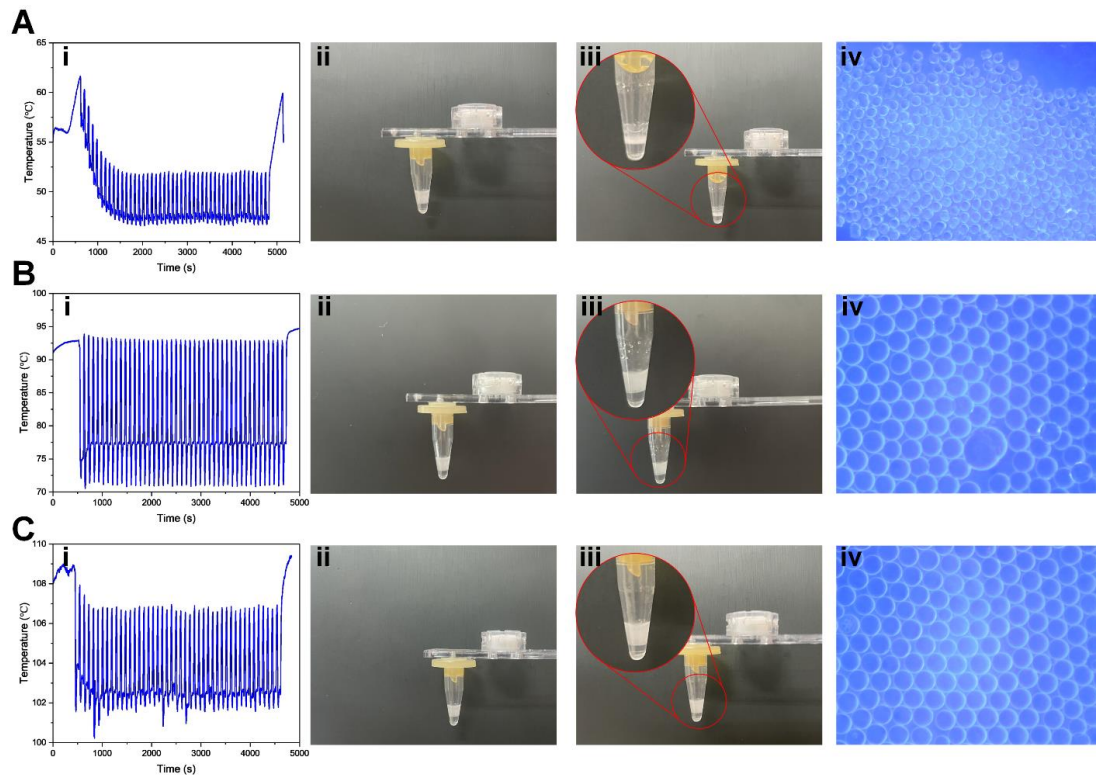


Figure S1. Comparative results of three experimental sets (A, B, C) each containing four Sub Figures. (i, ii, iii, iv). (A) The lid was not heated. (B) The annular heater was set to 100 °C. (C) The annular heater was set to 125 °C. (i) The temperature curves of air in the collecting tube during amplification. (ii) The droplets in the collecting tube before amplification. (iii) The droplets in the collecting tube after amplification. (iv) The droplets photos taken by a microscope.

Furthermore, experiments were conducted with the annular heater turned off, and then set to 100 °C and 125 °C, respectively. Photographs of the collecting tube were taken, and droplets were sampled for microscopic examination after amplification. The comparative results are depicted in Figure S1. From Sub Figure (ii) of Figures (A, B, C), it can be noticed that before amplification, the inner surfaces of the tubes are clean and free of droplets and liquid residues. When the annular heater is switched off, Sub Figure (i) in Figure S1(A) shows that the air temperature rises to a maximum of about 62 °C and falls to a minimum of about 47 °C, and during the denaturation-annealing-extension cycles, the temperature fluctuates between 47 °C and 52 °C. As seen in Sub Figures (iii) and (iv) in Figure S1(A),

the liquid level is lowered, the inner surface of the collecting tube has condensed and evaporated liquid, there is a large amount of condensed liquid under the lid, and the droplets under the microscope are poorly shaped, with non-circular boundaries and partially coalescence. This demonstrates significant droplet loss when the lid remains unheated. When the annular heater is set to 100 °C, Sub Figure (i) in Figure S1(B) shows that the air temperature rises to a maximum of about 95 °C and falls to a minimum of about 71 °C, and during the denaturation-annealing-extension cycles, the temperature fluctuates between 71 °C and 94 °C. The air temperature is slightly lower than the droplet temperature. We notice from Sub Figure (iii) in Figure S1(B) that there is still condensed liquid on the inner surface of the tube with liquid under the lid. In addition, droplets shape well under the microscope as shown in Sub Figure (iv) in Figure S1(B). This suggests that elevating the air temperature contributes to the reduction of droplet evaporation. When the annular heater is set to 125 °C, Sub Figure (i) in Figure S1(C) shows that the air temperature rises to a maximum of about 109 °C and falls to a minimum of about 100 °C, and during the denaturation-annealing-extension cycles, the temperature fluctuates between 100 °C and 107 °C. There is no obvious liquid on the inner surface of the tube, and the shapes of the droplets under the microscope are also good as illustrated in Sub Figures (iii) and (iv) in Figure S1(C), with no coalescence observed. These findings indicate that an air temperature exceeding the droplet temperature more effectively inhibits droplet evaporation.

Derived from the theoretical equations, a quantitative relationship between the mass evaporation rate and the temperature difference has been established, leading to the conclusion that the evaporation is suppressed when the air temperature is higher than the droplet temperature. Experimental measurements quantified the temperature inside the collecting tube, yielding data on the state of the collecting tube and the droplet morphology at different temperatures. This data also demonstrates that droplets are less prone to evaporation when the air temperature inside the collecting tube is elevated above droplet temperature.

2. Components of the automated ddPCR platform.

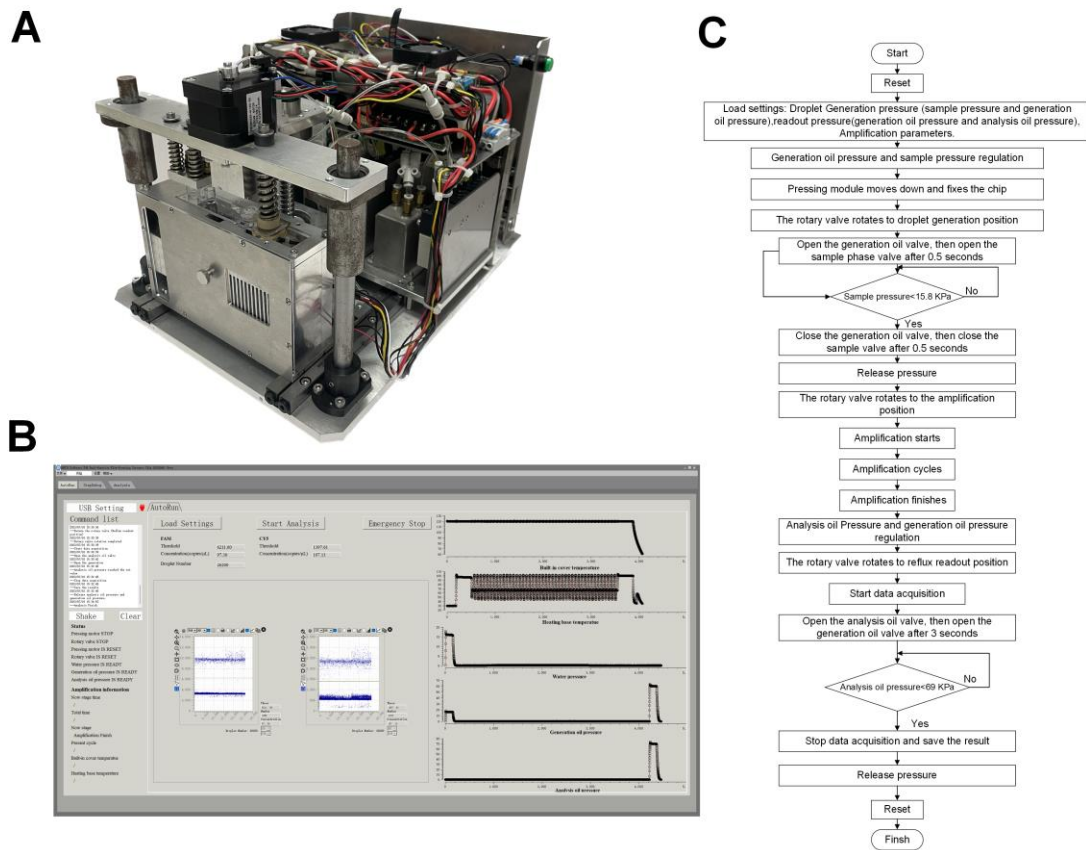


Figure S2. Components of the automated ddPCR platform. (A) The photograph of the device. (B) The software interface. (C) The flowchart of the program.

The automated ddPCR platform consists of the device (Figure S2(A)) and the software (Figure S2(B)) installed on a computer. The computer communicates with the device via a USB cable, realizing the device control and the data acquisition. Figure S2(B) shows the interface at the end of a ddPCR analysis. Figure S2(C) is the flowchart of the program in the software. The program runs following the flowchart when the 'Start Analysis' button is pressed.

3. The pressure recorded during the ddPCR analysis.

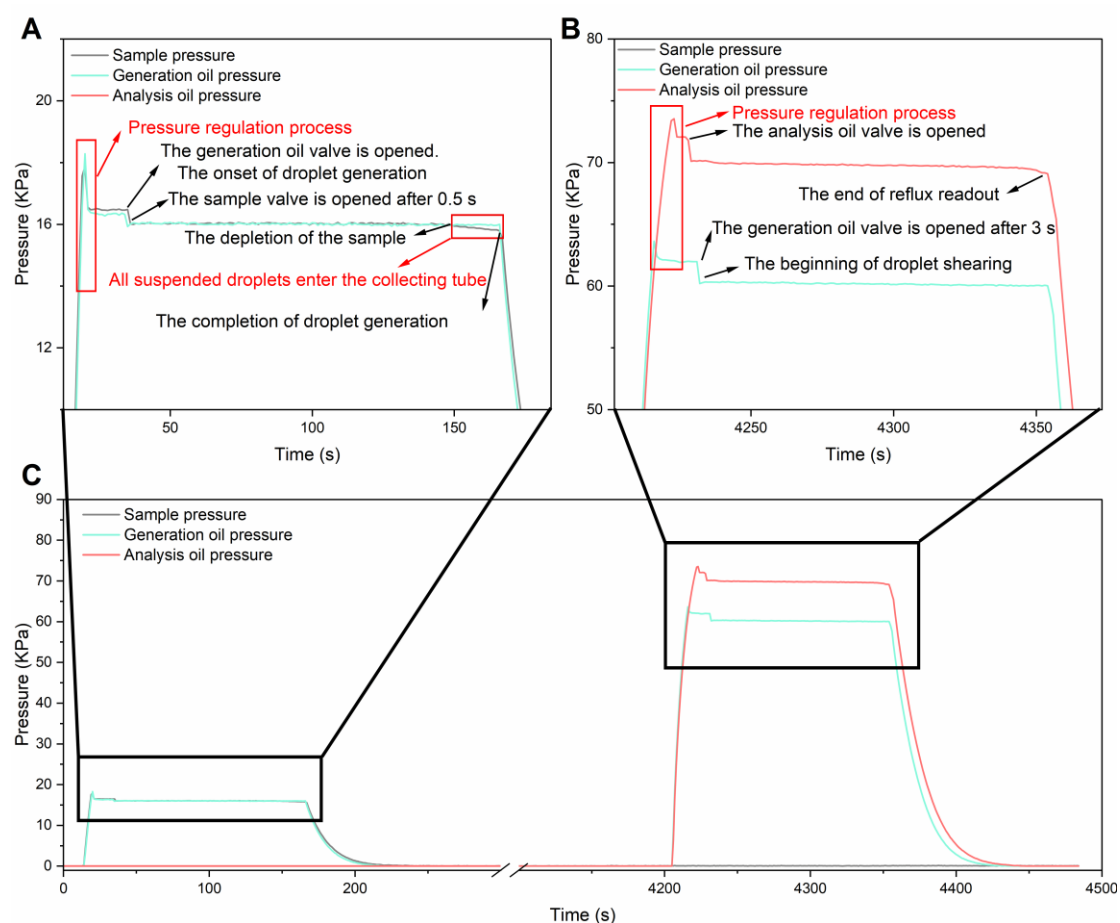


Figure S3. The pressure curves during the ddPCR analysis. (A) The pressure curves during droplet generation and the explanations of pressure variation. (B) The pressure curves during reflux readout and the explanations of pressure variation. (C) The pressure curves of the ddPCR analysis.

We designed three gas sources. The first one is used to drive analysis oil to push droplets into the micro-channels during reflux readout. The second one is used to drive generation oil for droplet formation and droplet separation at different stages, respectively. The third one is used to drive sample for droplet generation. Each gas source consists of a pump, three solenoid valves and an air tank. When pressure regulation, we firstly open the valve connecting the pump to the air tank, and we close the valve when the pressure is greater than or equal to the target value. If the pressure is greater than the target pressure, we open the valve which connects the air tank to a needle. Gas releases slowly through the needle, eventually the valve is not closed until the pressure is equal to the target value. The valve connecting the air tank to the chip will be opened or closed during different stages to apply pressure to the liquid. The pressure curves are as shown in Figure S3(C).

During droplet generation, the pressure curves are as shown in Figure S3(A). The pressure of sample and generation oil are regulated to both 16.5 KPa firstly. After the pressing module and rotary valve are executed. The generation oil valve is opened and the sample valve is opened after 0.5 s. The pressure drops to 16.0 KPa due to the pressure

balance among the gas tank, the tube and the chip. Since the volume of the gas tank is large enough (51,072 μL), the pressure remains constant during the whole process of droplet generation. The sample pressure continues to be applied to ensure that all droplets enter the collecting tube. When the sample pressure drops to 15.8 KPa, we close the valves then release the pressure in the gas tank, the droplet generation completed at this time.

During amplification, the collecting tube is sealed by the rotary valve, and we don't need to apply any pressure.

During reflux readout, the pressure curves are as shown in Figure S3(B). The analysis oil pressure is regulated to 72 KPa, and the generation oil pressure is regulated to 62 KPa. Here, the generation oil is used as shearing oil. The analysis oil valve is firstly opened. After about 3 second, the generation oil valves are opened. The oil pressure drops to 70 KPa and the generation oil pressure drops to 60 KPa after the valves are opened. Throughout the process, the analysis oil pressure slowly drops, and we stop the reflux readout when the analysis pressure reaches about 69 KPa. The pressure drop of 1 KPa had little effect on the reflux rate. Eventually, we release all the pressures.

4. The Thermodynamic simulation of the thermal cycler.

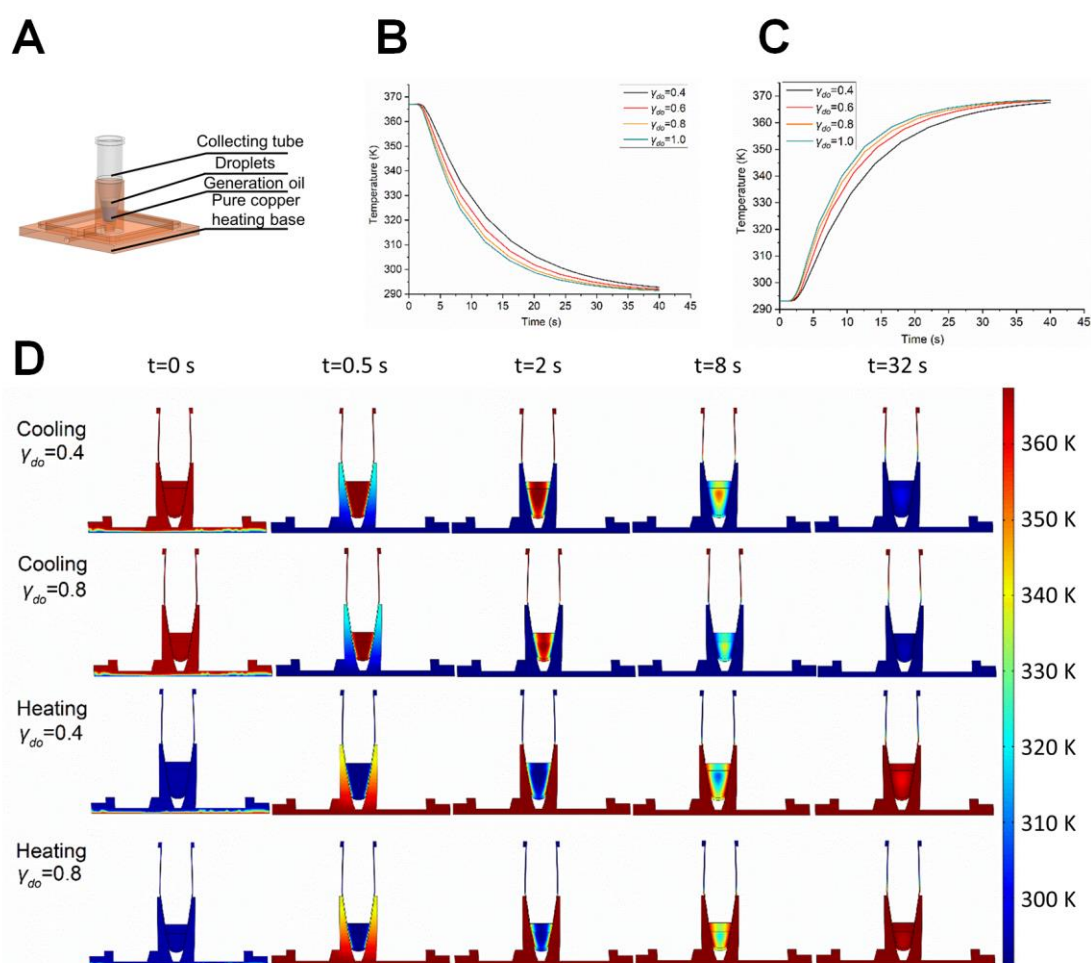


Figure S4. The Thermodynamic simulation results of the thermal cycler. (A) The simulation model of the thermal cycler. (B) Comparison of the temperature change rate of droplets at different γ_{do} during cooling. (C) Comparison of the temperature change rate of droplets at different γ_{do} during heating. (D) Thermodynamic diagrams at different times when γ_{do} is 0.4 and 0.8, respectively.

In order to explain the relationship between γ_{do} and the amplification efficiency in the thermal cycler, the relationship between γ_{do} and the rate of rising and cooling is simulated. As shown in Figure S4, the structure of the real expansion module is used as the simulation model, and the cooling or heating boundaries is set on the bottom surface of the heating base, respectively. We simulate the temperature change at the overall center of mass of the upper droplets at different γ_{do} , assuming that there is no heat exchange with the outside world.

The temperature curves under different γ_{do} are as shown in Figure S4(B) and Figure S4(C). The temperature change of the droplets is faster when γ_{do} is larger. In addition, the thermodynamic diagrams of the thermal cycler as the time goes on are shown in Figure S4(D) when γ_{do} is 0.4 and 0.8, respectively. We can see that the temperature starts to transfer from the side walls of the collecting tube to the center, and due to the conical structure of the collecting tube, a larger γ_{do} results in a larger area of contact between the droplets and the side walls, and at the same time, a closer distance between the droplets

and the heating base. In summary, we can obtain the conclusion that droplets are more likely to be heated or cooled when γ_{do} is larger and a larger γ_{do} can improve the amplification efficiency.

5. The principle of the Smith predictor for thermal cycle performance optimization

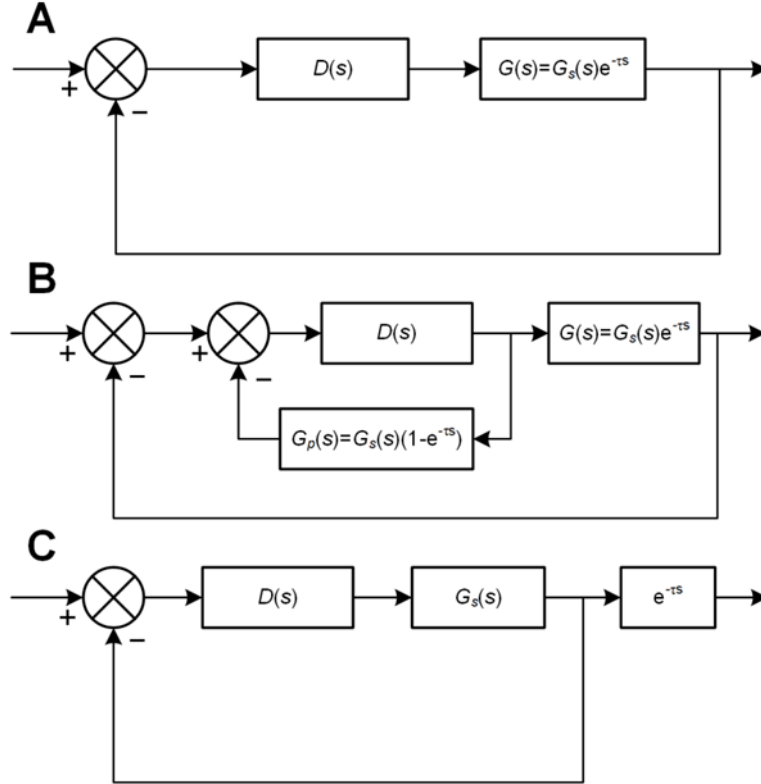


Figure S5. The temperature control system block diagram. (A) Closed loop control system block diagram without a Smith predictor. (B) Closed loop control system block diagram with a Smith predictor. (C) The equivalent closed loop control system block diagram with a Smith predictor.

The closed loop temperature control system block diagram in the thermal cycler is shown as Figure S5(A). $D(s)$ is a PID controller, $G(s)$ is the transfer function of the system, described as:

$$G(s) = G_s(s)e^{-\tau s} \quad (S3)$$

where s represents the complex frequency variable in the Laplace domain, τ represents the delay time constant, $G_s(s)$ is a first-order inertia element, and $G(s)$ is the transfer function of the system, which is the ratio of the Laplace transform of the output to the input. The closed loop transfer function without a Smith Predictor is described as:

$$\Phi_1(s) = \frac{D(s)G_s(s)e^{-\tau s}}{1 + D(s)G_s(s)e^{-\tau s}} \quad (S4)$$

where $\Phi_1(s)$ is the transfer function of the closed loop control system without a Smith Predictor. The pure time delay element ($e^{-\tau s}$) in the denominator changes the distribution of poles, thereby making bad effects on closed loop system's stability and dynamic performance. Therefore, a Smith predictor is introduced into the system. It is connected with $D(s)$ in parallel forming a negative feedback as shown in Figure S5(B). The transfer function of the Smith predictor is described as:

$$G_p(s) = G_s(s)(1 - e^{-\tau s}) \quad (S5)$$

The closed loop transfer function a Smith predictor is described as:

$$\Phi_2(s) = \frac{D(s)G_S(s)}{1+D(s)G_S(s)} e^{-\tau s} \quad (S6)$$

where $\Phi_2(s)$ is the transfer function of the closed loop control system with a Smith Predictor. The pure time delay element ($e^{-\tau s}$) in the denominator is eliminated. The equivalent system block diagram is drawn according to Equation S6, as shown in Figure S5(C). We found that the pure time delay element ($e^{-\tau s}$) is moved outside the closed loop. It does not affect the performance of the closed loop control system.

In conclusion, the Smith predictor has the capability to ameliorate the adverse effects caused by time delay.

6. The method of the threshold determination.

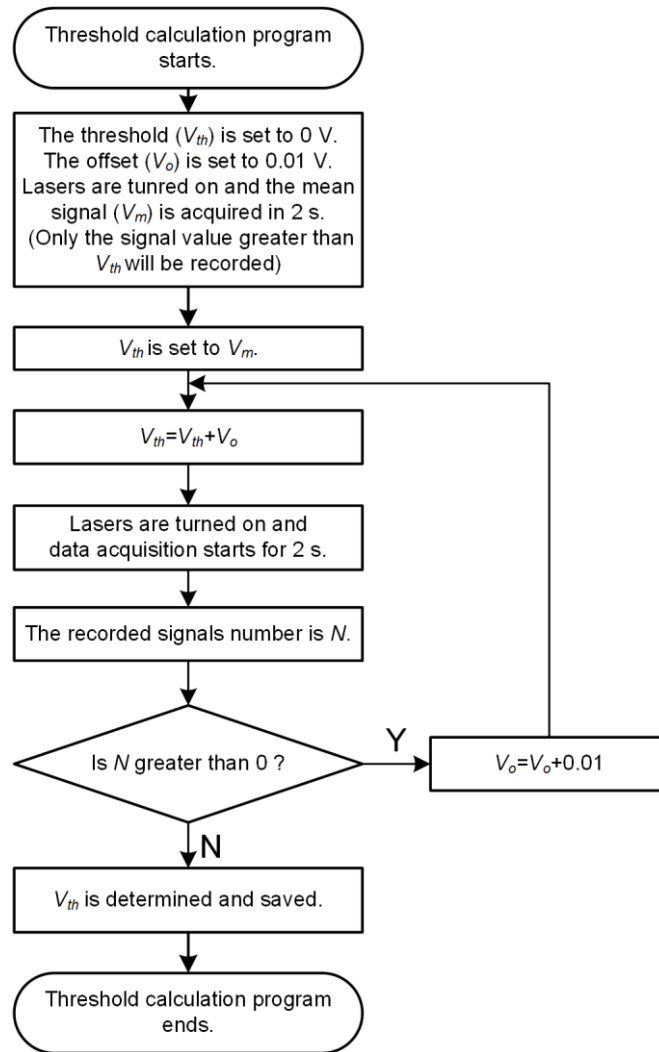


Figure S6. The flowchart of the threshold choice

The threshold is chosen as the program flow chart as Figure S6. In the threshold calculation program, the initial threshold is set to 0 V, and the initial offset (V_o) is set to 0.01 V. During signal acquisition, only the signal value greater than the threshold will be recorded. The mean background signal (V_m) is obtained in the first signal acquisition. Then, V_{th} is set to the sum of V_m and V_o . the program counts the number recorder after a new signal acquisition completes. If no signal is recorded, which indicates the threshold is greater than the noise. Therefore, the threshold is determined and the program ends. Otherwise, V_o is increased and the above process is executed again.

References:

1. J. H. Lienhard IV and J. H. Lienhard V, *A HEAT TRANSFER TEXT BOOK FOURTH EDITION*, 2017.
2. H. J. Palmer, *Journal of Fluid Mechanics*, 1976, **75**, 487-511.
3. W. K. Lewis, *Trans. ASME.*, 1922, **44**, 325-340.